Pushing the Boundaries: Enhancing TiO2 Performance for Hydrogen Evolution under Visible Light Photocatalysis by Incorporating RuO2

Journal:	*Sustainable Energy & Fuels*
Manuscript ID	SE-ART-01-2025-000040.R1
Article Type:	Paper
Date Submitted by the Author:	20-Mar-2025
Complete List of Authors:	Ashie, Mosses; North Carolina A&T State University, Chemistry Pathiraja, Gayani; University of North Carolina at Greensboro, Nanoscience; The University of North Carolina at Greensboro, Mantripragada, Shobha; North Carolina A&T State University, Joint School of Nanoscience and Nanoengineering Bastakoti, Bishnu; North Carolina A&T State University, Chemistry

Pushing the Boundaries: Enhancing TiO_2 Performance for Hydrogen Evolution under Visible Light Photocatalysis by Incorporating RuO_2

Moses D. Ashie[1], Gayani Pathiraja[2], Shobha Mantripragada[2], Bishnu P. Bastakoti[1]*
[1]Department of Chemistry, North Carolina A&T State University, Greensboro, NC 27411, USA

[2]Department of Nanoscience, Joint School of Nanoscience and Nanoengineering, University of North Carolina at Greensboro, 2907 East Gate City Blvd, Greensboro, NC 27401, USA

Email: bpbastakoti@ncat.edu

Abstract

A more efficient and highly porous TiO_2-RuO_2 nanocomposite was fabricated via a one-pot solvothermal route. Varying the amount of ruthenium content in the synthesis revealed the importance of synthesis condition modification in achieving a highly porous and effective photocatalytic material. Results from the study show that an optimal weight of 20% ruthenium precursor in TiO_2-RuO_2 nanocomposite demonstrated enhanced photocatalytic properties compared to other compositions. The nanocomposite exhibited a high performance in the H_2 gas evolution reaction due to the synergistic effect of TiO_2 and RuO_2, enhancing charge transfer and improving light absorption. The TiO_2-RuO_2-20 exhibited double reduction potential and low solution resistance. As a result of the reduced band gap, improved light absorption capability, and low electron-hole recombination, TiO_2-RuO_2-20 yielded a significant amount of hydrogen gas, 1794.8 $\mu molg^{-1}h^{-1}$, over 3 h of activity in visible light. This amount far exceeded the yield observed for the RuO_2 only (21.9 $\mu molg^{-1}h^{-1}$) and the commercially available TiO_2 (246.4 $\mu molg^{-1}h^{-1}$). This confirms the contribution and effectiveness of a low amount of ruthenium required in fabricating highly effective TiO_2-RuO_2 catalysts for photocatalytic hydrogen evolution. The single-step, low-cost solvothermal method offers a significant advantage in obtaining cost-effective materials for efficient hydrogen generation.

Introduction

Global exploration of efficient and long-lasting energy to meet the world's growing energy demand is on the rise due to modernization, innovation, automation, and industrialization[1]. The choice of energy sources has the potential to positively or negatively impact the environment and the economy, therefore drawing significant global attention into researching into energy sources that will positively impact society. Most of these energy sources such as coal, oil, and natural gas are non-renewable and releases carbon dioxide (CO_2) upon consumption which has negative environmental impact[2]. Hydrogen energy has been exploited as a potential energy source since the eighteenth and nineteenth century as was predicted by Jules Verne[3] that water will one day be exploited as a source of fuel. In recent times, hydrogen energy has been extensively investigated with photocatalytic water splitting as a clean and environmentally friendly route in hydrogen gas production compared to other methods. Photocatalysis which uses water, light including solar light, and catalyst is highly competing with the other generation methods such as steam methane reforming, biological, and electrolytic processes which releases CO_2, gives low production yield, and can be energy intensive respectively.

As a requirement for photocatalysis, water and solar light are abundant and renewable, leaving concern for a suitable photocatalyst to lower the theoretical minimum energy of ($\Delta G° = +237.13$ kJ/mol) or the minimum potential difference of (1.23 eV, $\Delta G°_{298K}$, 1 bar or 1.48 eV, $\Delta H°$) required to split water to produce hydrogen gas[4]. The photocatalyst plays a significant role in the absorption of light, charge separation, redox reactions, and lowering the activation energy. Titania's (TiO_2) undoubtedly role in photocatalysis for hydrogen evolution exploration has been extensively studied, with evidence of large band gap and high electron-hole recombination identified as potential limitations in its use as a photocatalyst[5,6]. Recent progress in this field has, therefore, seen much improvement in material fabrication for photocatalysis through modification via doping, composite formation, and control of surface characteristics through synthesis modification strategies. Modification of titania by doping with metals ($FeTiO_3$[7], V-TiO_2[8,9]), non-metals (N-TiO_2, SN-TiO_2, P-TiO_2)[10,11], co-catalysts (Ni, Pt, Co mixed with TiO_2)[12], composites (TiO_2-ZrO_2)[13] formation, and S- and Z-scheme creation[14,15] are a few examples of titanates engineered for photocatalysis. Most photocatalysts contain titanium due to its effective activity when modified, which enormously contributes to achieving a moderate band gap to absorb a considerable amount of light, generating charge carriers, lowering electron-hole recombination, and improving charge migration to active sites for effective photocatalysis.

Modifying titania via composite formation from binary metal oxide systems has the potential to enhance photocatalytic activity[16,17]. Aside from its multiple oxidation states, the incorporation of ruthenium in photocatalyst engineering has been observed to enhance light penetration in photocatalysts, flexible tunability of catalytic properties, and exhibition of a high degree of recyclability[18]. Ruthenium has been studied, and their complexes have also been known to act as good photosensitizers and photocatalysts due to the possession of the long-lived excited states phenomenon, which is a good redox property[18]. Through single-photon absorption, ruthenium has been identified as a facilitator in energy transfer, reduction, oxidation, and redox-neutral reactions in visible light irradiation[19]. Under low-energy near-infrared light irradiation (about 740 nm), ruthenium complexes demonstrate two-photon absorption properties, which play a significant role in driving photocatalytic reaction, modulating the weight of various constituent metals in a composite catalyst, and contribute significantly to obtaining the optimized material and understanding the unique properties of synthesized materials.[18]

Our work intends to improve the photocatalytic activity of titania TiO_2 for hydrogen generation by modifying TiO_2 with ruthenium and investigating the effect of regulating the amount of ruthenium on the physicochemical and photocatalytic properties of the fabricated material. The synthesis technique is designed to achieve a one-step, low-cost yet effective, and easy-to-reproduce synthesis technique. These investigations yielded a superb TiO_2-RuO_2 heterogeneous photocatalyst. It was synthesized through a solvothermal method using isopropyl alcohol and dimethyl formamide as a solvent mixture. This catalyst was found to have a high surface area and highly porous with excellent charge mobility. Several techniques, such as x-ray diffraction (XRD), Fourier transport infrared (FTIR) spectroscopy, x-ray photoelectron spectroscopy (XPS), electron microscopy, and Raman spectroscopy were used in characterization. Finally, the synthesized material was found to be a highly effective photocatalyst and yield a very high amount of hydrogen gas via water splitting in visible light.

Experimental

Materials

N, N dimethyl formamide (DMF), 99.9% from Fisher Chemical, titanium (IV) n-butoxide $Ti[O(CH_2)_3CH_3]_4$, 99% from Alfar Aesar, isopropyl alcohol (IPA), 100% v/v from LabChem, ruthenium (III) chloride hydrate ($RuCl_3.xH_2O$), 99.99% from Thermo Scientific and sodium sulfate decahydrate ($Na_2SO_4.10H_20$) from Acros Organics were used without further purification. Ruthenium (IV) oxide (RuO_2), 99.9%, and titanium (IV) oxide P25 (TiO_2) were purchased from Thermo Scientific and used as commercial comparative samples.

Synthesis of TiO_2 - RuO_2 nanocomposites

With stirring, 1 mL of titanium (IV) n-butoxide was added to a mixture of 30 mL IPA and 10 mL of DMF. 10 mg, 20 mg, 40 mg, 60 mg, and 100 mg of $RuCl_3$ were added to the resulting solution, stirred for 1 hour and heated in an autoclave at 180 ^oC for 20 h. The solution was allowed to cool to room temperature, washed with ethanol and dried in an oven at 60 ^oC. Samples prepared from 10 mg, 20 mg, 40 mg, 60 mg, and 100 mg of $RuCl_3$ were denoted TiO_2-RuO_2-10, TiO_2-RuO_2-20, TiO_2-RuO_2-40, TiO_2-RuO_2-60, and TiO_2-RuO_2-100 respectively. The pure TiO_2 was synthesized without using Ru precursor. The dried sample was calcined at 450 ^oC at a ramping rate of 3 ^oC/min for 2 h in OTF-1200X (MTI Corporation) tubular furnace.

Characterization

X-ray diffraction (XRD) patterns were obtained from an x-ray diffractometer (Rigaku; Miniflex 600 model), and the crystallite size of particles was calculated using the Debye Scherrer equation. The XRD spectra were obtained from 10° to 90° with a $Cu_{K\alpha}$ radiation (k = 1.5417 Å). The diffractometric investigations were carried out in ambient conditions at 2°/min scan rate, a step of 0.02°, an operational voltage of 40 kV, and a current of 15 mA. Elemental analysis and chemical bond interactions were performed using an x-ray photoelectron spectrometer (XPS, Escalab Xi+). Morphology was studied using a field emission scanning electron microscope (FESEM, Model JSM-IT800) and transmission electron microscope (TEM, Model JEOL JEM-2100plus) coupled with electron dispersive x-ray spectroscopy (EDX). ImageJ software was used to investigate the particle sizes and interplanar distances. Raman shifts, vibrational bands, and photoluminescence analysis were performed using a Raman confocal microscope (Horiba) and Fourier transform infrared spectrometer (FTIR). Shimadzu IRTracer-100 spectrophotometer equipped with a DLATGS detector was used in recording FTIR spectra from 400–4000 cm^{-1}. BET (Brunauer-Emmett-Teller) surface analysis was performed using TriStar II Plus 3.03 (Micromeritics) BET instrument. DiffusIR reflectance accessory (PIKE Technologies) fitted in a UV-Vis spectrometer (Evolution Pro, EV3Z315002, Thermo Scientific) aided in recording the fabricated materials' light absorption and reflection properties.

Electrochemical characterization

The synthesized photocatalysts were coated on a copper substrate, and the electrochemical behavior was studied using the CH Instrument workstation. A mixture of 4 mg of finely powdered photocatalyst, 0.5 mL of ethanol, and 50 µL of Nafion solution was sonicated for 1 h. The resulting solution was deposited on the Cu substrate to form 1 cm^2 area electrode and dried at 60 °C for 4 h. Electrochemical Impedance, cyclic voltammetry, flat band potential, and stability of the materials were investigated in a three-electrode system (Cu substrate as a working electrode, platinum electrode as a counter electrode, and Ag/AgCl electrode as a reference electrode) in a 0.5 M Na_2SO_4 electrolyte at room temperature. A transient current switched on-and-off test was performed using an amperometry technique and solar light irradiation of AM 1.5G from the solar simulator at an intensity of 200 $mWcm^{-2}$.

Photocatalytic Testing

The photocatalytic hydrogen evolution capacity of the fabricated material was investigated using a closed glass reactor set-up (pyrex glass) in ambient conditions. The 165 mL capacity reactor is enclosed in a dark box to avoid interference of surrounding light. During an experiment, 30 mg of catalyst is added to 50 mL of 10% methanol solution in deionized water as the reaction medium with magnetic stirring at 250 rpm. The reactor was purged with nitrogen gas for 5 min, and the solution was irradiated with solar light from a solar simulator for 3 h in a quartz evacuated outer chamber. The solar simulator, model PEC-L01, (AM 1.5 G, 200 mW cm^{-2}) was applied to provide modeled solar light through a 4 cm x 4 cm quartz window. The Xe lamp of the solar simulator emits light across a range of approximately 350 nm to 1100 nm. The temperature within the reactor was monitored using an infrared temperature detector (Custom IR-300), and the light intensity of 254.9 kLux (2013.7 W/m^2) used was measured using the Light Meter LT300 (Extech Instruments).

The well-sealed reactor is continuously stirred throughout the experiment and the temperature controlled by circulating water and adjusting temperature to 50 °C with a BAC heating pad. The hydrogen gas evolved was quantified using a gas chromatograph (SRI; 8610C) coupled with a thermal conductivity detector. Argon gas is used as a carrier gas.

Results and Discussion

The solvothermal synthesis technique was a unique method yielding highly porous heterogeneous TiO_2-RuO_2 nanocomposite (**Fig. 1**). DMF and IPA serve as solvents, and the wide solubility range of DMF[20,21,22] makes it more favorable for the dissolution of titanium (IV) n-butoxide, which is soluble in a non-polar solvent, and the ruthenium (III) salt, which is soluble in a polar solvent. The ability of DMF to act as a ligand[23,24] enables coordination with the multivalent positive metal ions (Ti^{4+}, Ru^{3+}), effectively dispersing them into a solution. The presence of lone pairs acts as Lewis base sites[25], inducing strong, attractive forces, coordinating with the metal ions and further enhancing the dispersal of metal species. These aid in obtaining well-dispersed particles during thermal treatment for the hydrolysis of metal ions, nucleation, growth, and crystallization of the NPs, enhancing porosity, and preventing agglomeration. At appropriate synthesis and solvation conditions, these molecules contribute effectively to the orderly self-assembly, growth, and control of the size of the nanoparticles.

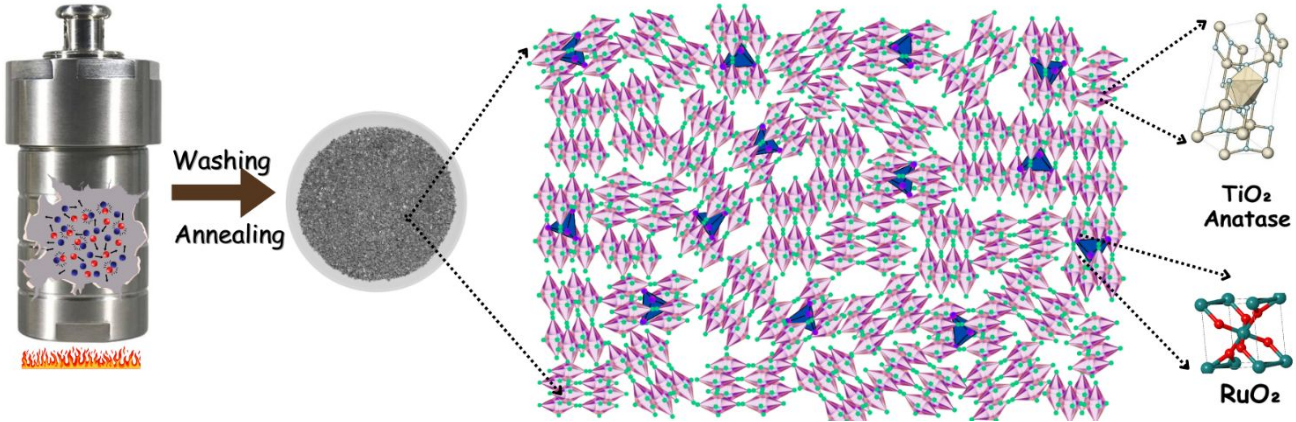

Fig. 1. Schematic illustration of the synthesis of highly porous TiO_2-RuO_2 by one-pot solvothermal method.

XRD (**Fig. 2a**) provided crystalline information with crystal lattice phases separately matching with anatase TiO_2 (standard PDF no. 00-021-1272 having I41/amd (141) space group) and tetragonal crystal structure of RuO_2 (standard PDF no. 04-009-7842 having P42/mnm (136) space group). The distinct XRD peaks from TiO_2 and RuO_2 confirm that Ru is not incorporated into the lattice of TiO_2, indicating the formation of a nanocomposite (**Fig. 2a-b, Fig. S1-2**). Crystal sizes were observed to range between 9.24 and 13.63 nm as calculated from XRD using the Scherrer equation (**Table S1**). Infrared vibrational bands at 1122.6 cm^{-1} and 1467.7 cm^{-1} can be attributed to C-N stretching modes[26], and bands at 1656.5 cm^{-1} can be attributed to C=O stretching modes from DMF (**Fig. 2c**). These components and functional groups were removed after annealing at 450 °C.

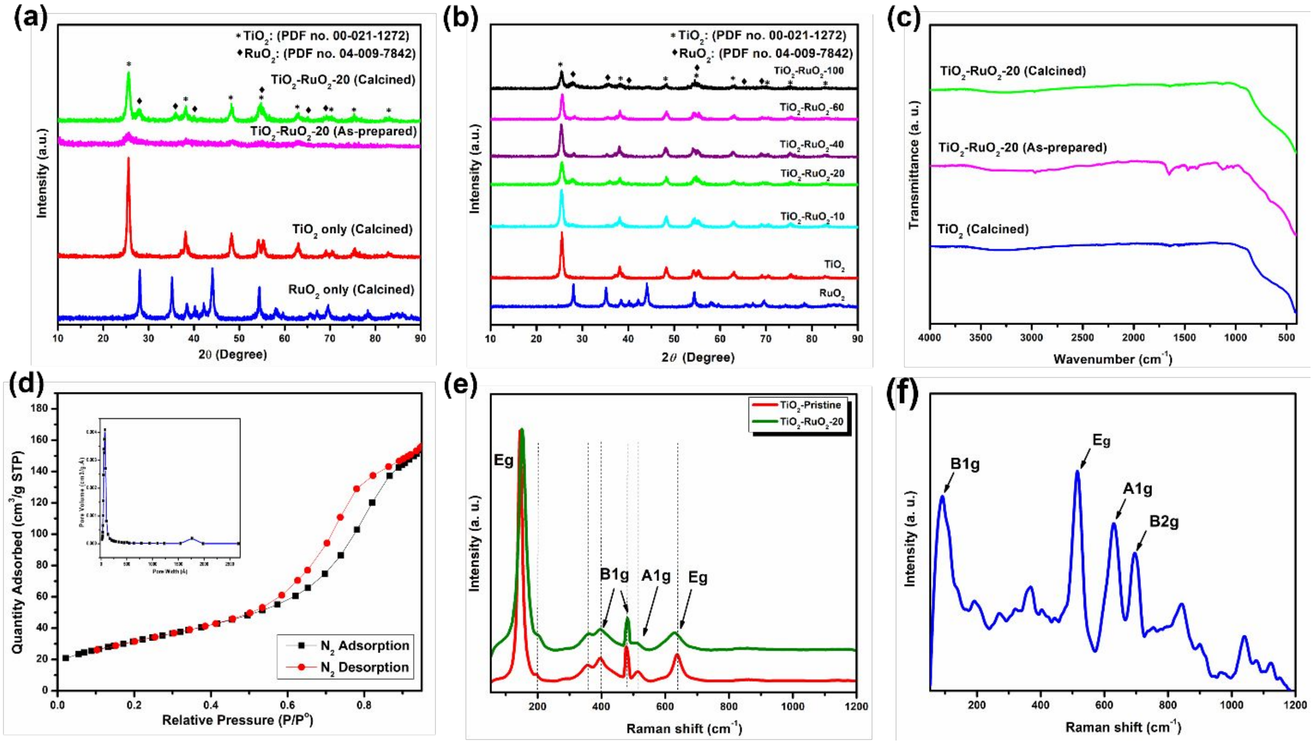

Fig. 2. a) XRD of TiO_2, RuO_2, and TiO_2-RuO_2-20, (b) XRD spectrum of TiO_2, RuO_2, and all TiO_2-RuO_2 samples calcined at 450°C. (c) FTIR spectrum of TiO_2-RuO_2-20 before and after calcination, (d) BET analysis result of TiO_2-RuO_2-20, (e) Raman shift of TiO_2 and TiO_2-RuO_2-20, and (f) Raman shift of RuO_2 samples.

BET analysis confirmed that the synthesized nanocomposites have a high surface area (115.42 m^2g^{-1}), exposing more active sites for the catalytic reaction. The pore size distribution (insert of **Fig. 2d**) showed that the average pore diameter lies between 10 and 15 nm, indicating mesoporosity. Raman vibrational modes obtained confirmed that the crystal lattice of TiO_2 remained unchanged in the presence of ruthenium. Vibrational bands were observed at 144.6 cm^{-1} (Eg), 196.4 cm^{-1} (Eg), 398.6 cm^{-1} (B1g), 518 cm^{-1} (A1g), and 638.6 cm^{-1} (Eg) which are characteristic of anatase TiO_2 with no rutile phase. The Eg bands arise from symmetric stretching vibrations of O-Ti-O bonds in TiO_2, while A1g and B1g occurred due to symmetry and anti-symmetric vibrations of O-Ti-O bonds in TiO_2, respectively. No significant shift in A1g and B1g bands was observed between the pure TiO_2 and the TiO_2-RuO_2-20 sample, as shown in **Fig. 2e**. The broadening and shifting of peaks in the Eg band of the composite to a higher wavelength from 144.6 cm^{-1} to 151.3 cm^{-1} could be attributed to a reduction in particle size and bond length resulting in phonon confinement, thereby altering the vibrational properties of the composite[27]. The contribution of peaks from B1g, Eg, A1g, and B2g bands of RuO_2 (**Fig. 2f**) located at 90.2 cm^{-1}, 515.2 cm^{-1}, 629.4 cm^{-1}, and 695.9 cm^{-1} respectively also resulted in broadening of peaks in the composite.

Field emission scanning electron microscopic (FESEM) assessment of nanocomposites revealed porous nanoparticles formed from smaller particles about 30 nm and orderly arranged (**Fig. S4-S9**). Microscopic imaging revealed the highly fragmentable nature of the nanoparticles, appearing as loosely bonded particles with some particles joining to form uniform single nanostructures. It is, however, noticeable from BET results that there was increase in surface area for the RuO_2 -TiO_2-20 material after the composite formation (**Fig. S10** and **Table S2**). This strongly contributed to increased active sites, leading to high water splitting performance compared to the other samples. The structural and crystallinity analyses confirmed the presence of RuO_2 and TiO_2 in all samples, further confirmed by HRTEM. **Fig. 3** shows the morphology of synthesized particles, crystallinity, and chemical composition using HR-TEM/STEM EDX analysis. The HR-TEM image evidences the formation of larger aggregated microspheres (**Fig. 3a**). The crystal lattice spacing values of RuO_2-TiO_2 microspheres are found to be 0.33 nm, which are oriented in the (110) direction and 0.23 nm towards (020) crystal planes in this sphere, corresponding to RuO_2 and TiO_2, respectively. These are in good agreement with the literature values [28,29,30]. Its selected area electron diffraction (SAED) pattern consists of a characteristic ring pattern with many brighter spots representing Bragg's reflection of each crystallite. This further confirms the polycrystalline nature of these microspheres, as shown in **Fig. 3c.** The STEM combined with EDX analysis reveals the distribution of each metal oxide in the RuO_2 -TiO_2 composite. Its angular-dark field-scanning transmission electron microscopy (ADF-STEM) image (**Fig. 3d**) further demonstrated the elemental distribution of Ru, Ti, and O in the composite (**Fig. 3e**), and the corresponding elemental maps (**Fig. 3f–h**) confirm the presence of a higher percentage of Ti compared to Ru according to its chemical composition and the homogenous distribution of Ru crystals in the nanocomposite. Crystal lattice investigation using ImageJ revealed some orderliness in the crystal arrangement of the of TiO_2 (**Fig. 3j**) and some form of lattice disorder (**Fig. 3k**) in the RuO_2 lattice fringes as measured at different points in the crystalline nanoparticles. This could possibly be attributed to defects in the RuO_2 crystals.

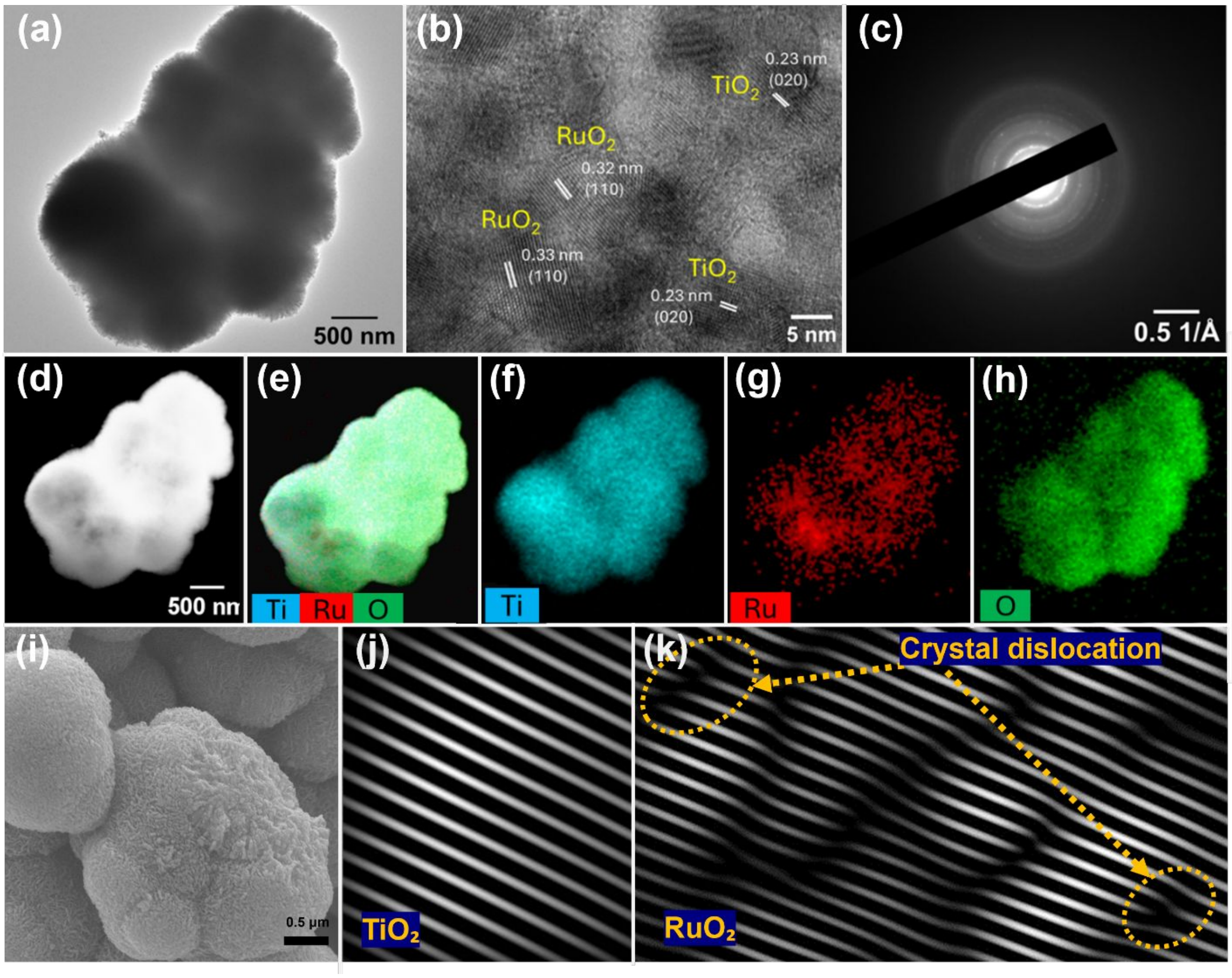

Fig. 3. (a) HR-TEM image of RuO_2-TiO_2 microspheres (low magnification) (b) HR-TEM image taken at 400kx, showing lattice spacings of RuO_2 and TiO_2 crystals (c) SAED of microspheres (d)

its ADF-STEM image; (e) corresponding EDX overlay elemental map, and (f–h) individual elemental mapping for Ti, Ru, and O, respectively; (i) SEM image; (j) FFF inverse image of ImageJ showing crystal lattices of TiO_2; and (k) FFF inverse image of ImageJ showing crystal lattices of RuO_2 of the TiO_2-RuO_2-20 sample with crystal defects.

XPS analysis revealed the chemical composition and oxidation states in the nanocomposites. Survey scans performed on the pristine TiO_2, RuO_2, and the composite showed peaks corresponding to Ti 2p, Ru 3d, and O 1s (**Fig. 4a, Fig. S12)**. XPS spectra of Ti 2p from the pristine TiO_2 shows the presence of Ti $2p_{3/2}$ and Ti $2p_{1/2}$ at 458.59 eV and 465.26 eV, respectively, with an area ratio of 2.08:1.00 (**Fig. S11**) agreeing with the doublet spin states of the p orbitals of Ti and correspond to Ti^{4+} oxidation state[9]. The Ti^{3+} oxidation state exists at lower binding energy (BE) of about 457 eV[31]. The Ru $3d_{5/2}$ and Ru $3d_{3/2}$ peaks of pristine RuO_2 with a BE of 279.5 and 285.3 eV yielded an area ratio of 3.5:2 (**Fig. S11**). Spectra peaks at 283.54 eV and 287.01 eV in Ru 3d (**Fig. 4b)** relates to the Ru^{4+} oxidation state[32] with slight shifting in BE which could be due to C1s interference[33] from binder on substrate. The separation of 5.71 eV is observed between Ti $2p_{3/2}$ and Ti $2p_{1/2}$ peaks representing the spin-orbit splitting and agrees with literature 5.7-6.2 eV[34]. A strong shift in binding energy observed for the Ru 3d in the deconvoluted peaks at 283.77 eV and 285.28 eV can be attributed to lattice defects in the RuO_2 and strong interaction with TiO_2 in the composite. The BE observed at 287.01 eV, 288.82 eV can be attributed to C interference[33] from the substrate due to low intensity of the RuO_2 species. The peak at 531.42 eV from the O 1s high-resolution spectrum (**Fig. 4c)** is typical of surface hydroxyl (–OH) groups[7], which is comparable to that in the pristine TiO_2 peak at 531.62 eV. The significant shifting in BE in the Ru 3d of the composite reveals a strong interaction between the TiO_2 and RuO_2 metal oxides due to strong bonding effect experienced by the RuO_2 from the surrounding TiO_2 crystals. Shifting in BE in Ti 2p is also observed in the composite and the pristine TiO_2, indicating some degree of chemical interaction between the RuO_2 and TiO_2 lattice.

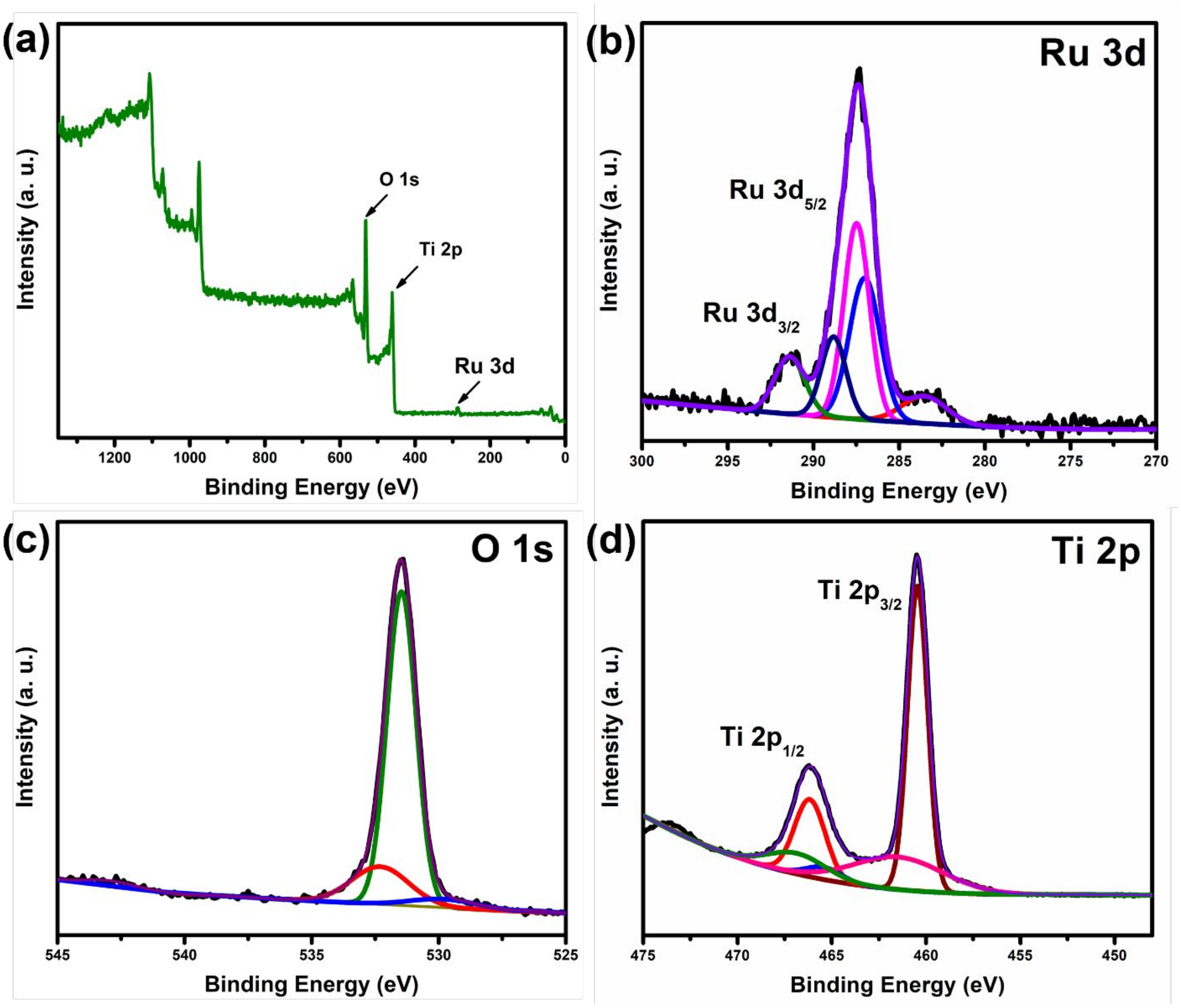

Fig. 4. High-resolution XPS analysis results of a) Ti 2p, b) Ru 3d, c) O 1s, and d) comparison of binding energies of Ti 2p in the composite and the pristine TiO_2.

Diffuse reflectance and photoluminescence analysis were performed to investigate the light absorption and emission properties of the nanocomposites. Results indicated strong light absorption capacity (**Fig. 5a**) by the TiO_2-RuO_2 composites favoring photocatalytic activity in the visible light region compared to the commercially available TiO_2 having low absorption in the visible light region after 400 nm. All samples exhibited an indirect band gap below 3.0 eV, as indicated in (**Table S2** and **Fig. S13**). The pristine TiO_2 exhibited a reduced band gap, which can be attributed to enhancement in surface properties due to the solvothermal synthesis technique. The pristine TiO_2 sample exhibited an improved band gap of 2.93 eV as compared to the commercial TiO_2 (3.18 eV). Synergistically, the composite formed between RuO_2 and TiO_2 aided in achieving an optimally stable TiO_2-RuO_2-20 sample exhibiting an indirect band gap of 2.91 eV.

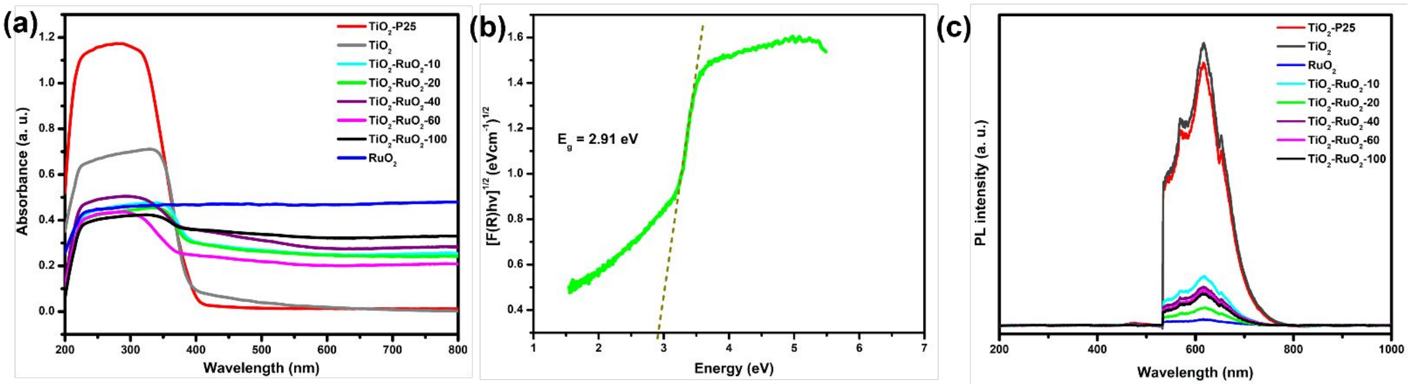

Fig. 5. a) UV-visible diffuse reflectance spectroscopic absorption spectra of TiO_2-RuO_2 composites, b) Band gap determination of TiO_2-RuO_2-20, and c) PL spectra of pristine TiO_2, pristine RuO_2 and TiO_2-RuO_2 samples compared with commercially available titanium dioxide (TiO_2-P25).

Very low emission characteristics (**Fig. 5c**) in the synthesized samples compared to the pristine TiO_2 were observed in the emission spectrum. Photoluminescence (PL) results of the TiO_2-RuO_2-20 sample showed a lower emission spectrum, indicating a slow electron-hole recombination rate, thereby enhancing the transfer of photogenerated charges for adequate water-splitting activity. The PL test was carried out at excitation wavelengths of 532 nm, and scanned within an energy range of 1.5 eV to 6.2 eV (800 nm to 200 nm) using the Raman instrument[35]. Light absorption is significantly improved in the visible region of the electromagnetic spectrum, and light emission is substantially reduced; this confirms why our material was highly efficient under visible light irradiation.

Further investigation to understand the electronic properties of the nanocomposites revealed high electrochemical characteristics exhibited by the TiO_2-RuO_2-20 sample, contributing to its high photocatalytic performance. The electrochemical cyclic voltammetry technique was employed to verify the oxidative and reductive potential of the fabricated materials at a scan rate of 50 mV/s. Though most materials showed higher reduction potential, TiO_2-RuO_2-20 exhibited double reduction peaks (**Fig. 6a** and **Fig. S14)**. Compared to the other materials, the TiO_2-RuO_2-20 sample exhibited a double reduction potential at ≈ -0.08 V and ≈ -0.38 V. This indicates that

TiO_2-RuO_2-20 material will undergo sequential and reversible reduction steps, transferring one electron in each step, contributing to high electron density. This was confirmed, as the TiO_2-RuO_2-20 sample outperformed in photocatalytic activity.

The n-type semiconductor characteristics exhibited by the nanocomposites were tested through impedance potential analysis, and data were analyzed using a Mott-Schottky plot (**Fig. 6b**). Results indicating flat band potential at different frequencies have been shown in **Fig. S15** and **Table S4**. From the results, the TiO_2-RuO_2-20 sample displayed a flat band potential of -0.91 V vs. Ag/AgCl electrode converted to -0.71 V vs. NHE. The positive slope from the Mott-Schottky plot confirms that our synthesized materials exhibited an n-type semiconductor behavior. This n-type behavior can be attributed to the electron-rich nature of RuO_2 in the composite, with electrons from its 4d spin-orbital coupling contributing to its electronic properties. Moreover, RuO_2 is known to be a good conductor due to the high density of charge carriers[36]. During the hybridization of RuO_2, the Ru^{4+} oxidation state of ruthenium results in a donation of 4 electrons to oxygen, and the remaining electrons in the d-orbitals contribute to the electronic properties of RuO_2. After irradiation of light, electronic transitions due to energy absorbed can contribute to the variable oxidation state of ruthenium thereby enhancing the photocatalytic properties of the catalyst. During photocatalysis, the oxidation state of ruthenium has been reported to change from Ru^{3+} to Ru^{4+} as applied potential increases[37].

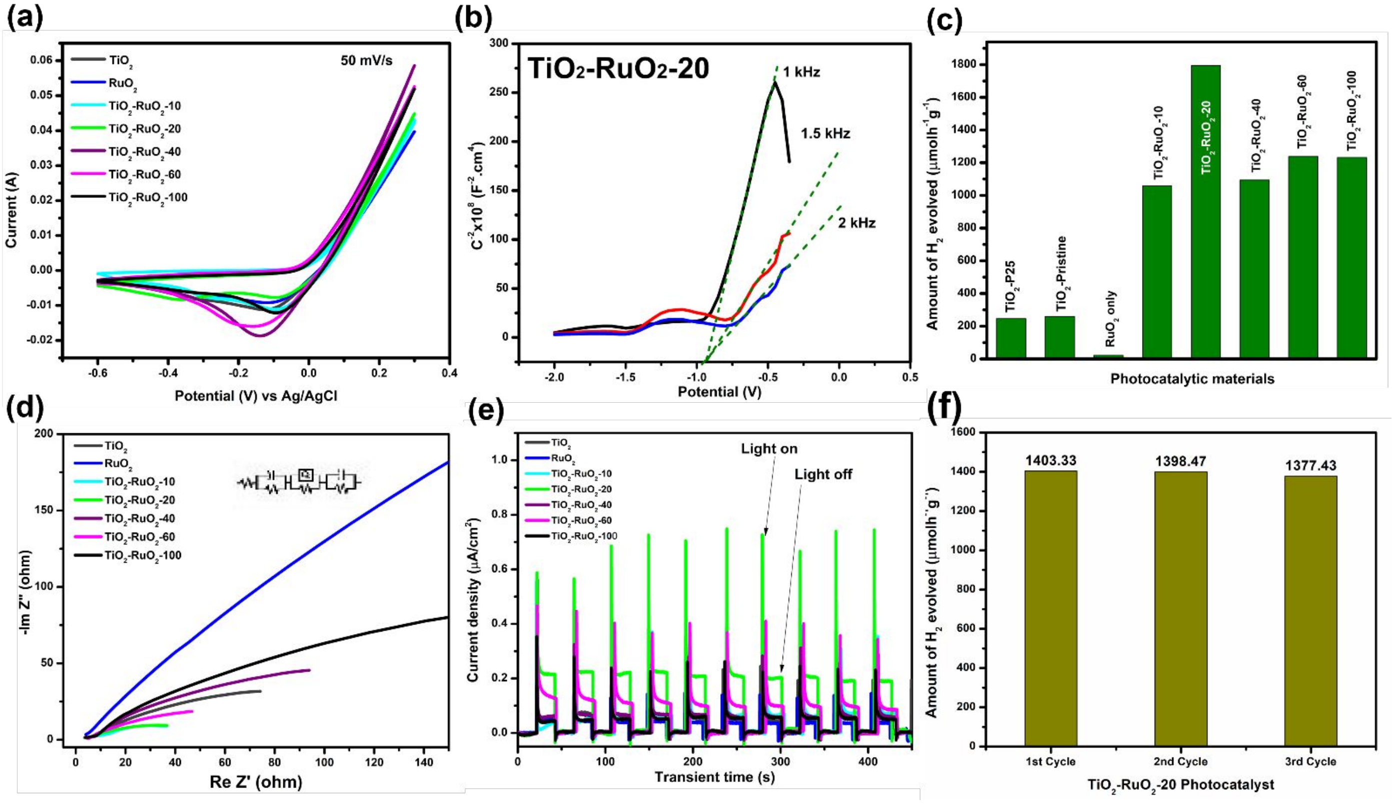

Fig. 6. a) Cyclic voltammetry, b) Mott–Schottky plot for the electrochemical impedance potential spectroscopic investigation at a frequency of 1 kHz, 1.5 kHz and 2 kHz. Investigated in a three-electrode system using the synthesized material on a Cu substrate as working electrode, platinum electrode as a counter electrode, and Ag/AgCl electrode as reference electrode in a 0.5 M Na_2SO_4 electrolyte in ambient conditions, c) Evaluation of photocatalytic hydrogen production performance for different samples, d) Nyquist plot, e) On-and-off transient current test of TiO_2-RuO_2 samples, and f) Stability results of TiO_2-RuO_2-20 sample after 3 cycles.

Simulated results from electrochemical impedance spectroscopic (EIS) studies show all samples displaying equivalent circuit diagrams except for RuO_2 and TiO_2-RuO_2-20 (insert in **Fig. 6d**). The simulation results of the TiO_2-RuO_2-20 sample showed a lower solution resistance compared to the other samples. The low TiO_2-RuO_2-20 sample solution resistance strongly indicate free and rapid transport of charge carriers for photocatalytic activity. The TiO_2-RuO_2-20 sample with lower charger transfer resistance will, therefore, demonstrate effective charge transfer in an electrolyte. This confirms why the TiO_2-RuO_2-20 sample outperforms all the other synthesized materials in the photocatalytic hydrogen evolution. The TiO_2-RuO_2-20 sample showed an effective response to visible light irradiation (**Fig. 6e**), exhibiting a high current density of 0.22 μA/cm^2. A switch-on-and-off transient photocurrent test was employed to investigate the possible charge conductivity property and charge transfer resistance of the electrode-electrolyte interface of our fabricated material. The high current density of 0.22 μA/cm^2 far exceeded the results obtained from the other samples confirming its unique performance in hydrogen generation reaction.

TiO_2-RuO_2-20 sample yielded 1794.8 μmolg^{-1}h^{-1} of hydrogen gas as compared to 1058.0, 1093.8, 1237.8, 1231.7 and 21.9 μmolg^{-1}h^{-1} recorded for TiO_2-RuO_2-10, TiO_2-RuO_2-40, TiO_2-RuO_2-60, TiO_2-RuO_2-100 and RuO_2 only samples respectively. The solar light provided a more consistent means of mimicking the sun for photocatalytic hydrogen evolution activities. The possible presence of lower UV wavelength photons contributed to a significant amount of gas generated by the TiO_2. Light Meter LT300 recorded an intensity of 254.9 kLux (2013.7 W/m^2), which is equivalent to 2 suns. The recoverability and re-usability of the photocatalyst were investigated after 2 h of hydrogen evolution for the TiO_2-RuO_2-20 sample. After a third cycle, the TiO_2-RuO_2-20 sample exhibited excellent stability **(Fig. 6f)**. XRD and FTIR characterization results show no significant difference between the initial sample and the sample after the final cycles indicating that the TiO_2-RuO_2-20 photocatalyst is chemically stable for reuse in catalyzing hydrogen production under solar light irradiation. Individually, the other samples exhibited low amount of hydrogen which can be attributed to the low light absorption capacity and low current density in photocurrent switched on-and-off experiment in visible light. The high emission observed in the PL test also confirms the high electron-hole recombination of TiO_2 as previously reported[38]. Though RuO_2 exhibited high light absorption capacity, it produced low current density in photocurrent switched on-and-off experiment in visible light with high emission observed in the PL test. The TiO_2-RuO_2-20 sample, therefore, exhibited effective photocatalytic properties, high hydrogen evolution capacity, and high stability for a long-term usage.

The mechanism of photocatalytic activity was proposed to understand the photocatalyst's charge generation and charge transfer activities. Based on experimental results from this study, a proposed mechanism that ensured enhanced water splitting in the presence of TiO_2-RuO_2 composite nanoparticles is illustrated in **Fig. 7**. The work function (Φ) which is an important factor for charge transfer between semiconductor interfaces is measured using equation 1.

$$\Delta V = \Phi - \varphi \qquad (1)$$

where: ΔV is the contact potential difference, and measured from the distance between inflection points, IP1 and IP2, on the XPS Valence Band (XPS-VB) spectrum.

Φ is the work function of the sample measured in a small angle

φ is the work function of the tester and has a value of 4.55 eV[39]

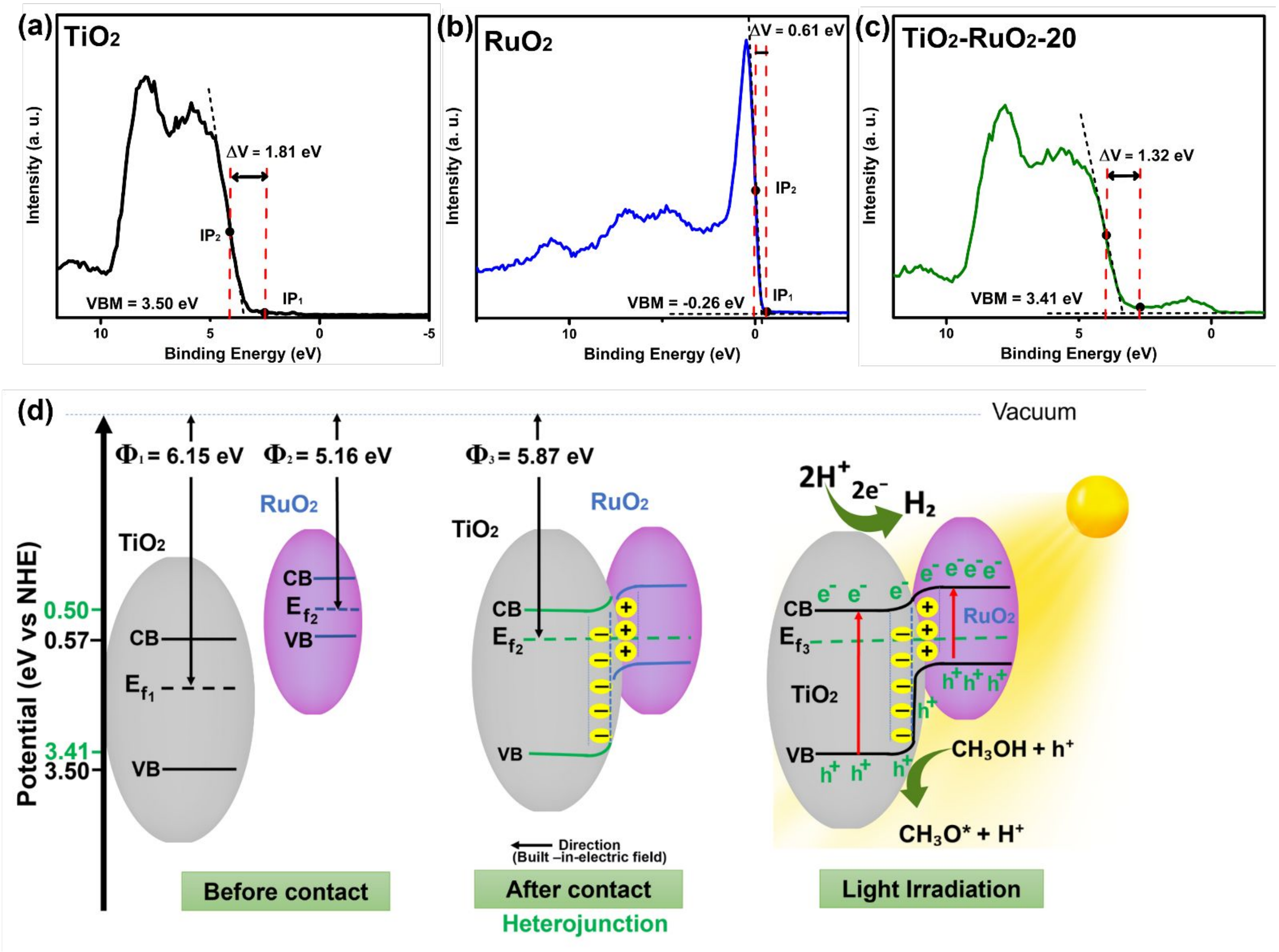

Fig. 7. (a-c) Schematic illustration of the XPS-VB determination of Valence Band maxima (VBM), and (d) mechanism of formation of IEF and photocatalytic hydrogen evolution using TiO_2-RuO_2 composite nanomaterial.

From the XPS-VB analysis results, ΔV values of 1.60 eV, 0.61 eV, and 1.32eV resulting in Φ values of 6.15 eV, 5.16 eV, and 5.87 eV were obtained for the TiO_2, RuO_2 and TiO_2-RuO_2-20 samples respectively. The work function of RuO_2 agrees with literature which is approximately equal to 5.2 eV[40,41]. The more negative position of the valence band maxima (VBM) in the RuO_2

spectrum indicates overlap between VB and CB which confirms the metallic nature of the RuO_2[42]. The conduction band energies (E_{CB}) were also measure using equation 2.

$$E_{VB} = E_g + E_{CB} \tag{2}$$

With measured band gap energies (Eg) of 2.93 eV, 1.33 eV, and 2.91 eV, E_{CB} values of 0.57 eV, -1.61 eV, and 0.50 eV were respectively obtained for the TiO_2, RuO_2 and TiO_2-RuO_2-20 samples. The variation in work function and other parameters between the individual materials and composite shows a strong interfacial interaction at the heterojunction of the composite. When combined, RuO_2 with the low work function[43] will cause continuous flow of electrons to the TiO_2 until the Fermi energy levels reach equilibrium[44]. In the process, an electron accumulation layer and electron depletion layer will respectively be formed near the interface between the TiO_2 and the RuO_2, causing RuO_2 to be positively charged and TiO_2 negatively charged. This will result in an internal electric field (IEF)[45] directed from RuO_2 to TiO_2. The loss of electron will cause RuO_2 bend downwards with TiO_2 bending upwards. The IEF created will enhance transfer of photogenerated electrons from the CB of the RuO_2 to the CB of the TiO_2 after light irradiation. This S-scheme heterojunction importantly contributes to separating photogenerated electrons and holes preventing electron-hole recombination[46]. As a result, the retained charge carriers can participate in photocatalytic water splitting to generate hydrogen gas. The wide wavelength range of the Xe lamp in the solar simulator extending to about 350 nm enables the absorption of some amount of UV radiation to slightly contribute to generation of charge carriers to increase photocatalytic activity. The presence of methanol in the reaction medium will scavenge holes and ensure continuity in the photocatalytic hydrogen reaction, as shown schematically in **Fig. 7**. Electrons available in the photocatalyst-electrolyte interface effectively participate in reducing protons (H^+) to hydrogen (H_2). At the same time, holes migrate to the catalyst's surface and are scavenged by the methanol to ensure continuous redox activity. The working electrode of the TiO_2-RuO_2-20 was also very stable (**Fig. S16)** after 23 hours. Other characterizations performed such FTIR, XRD, and XPS (**Fig. S17-S19)** on the samples after the hydrogen experiments shows that the photocatalyst is very stable.

Conclusion

This work revealed the vital role of ruthenium in modifying the photocatalytic properties of TiO_2. Adjusting the weight of ruthenium induced better physical and chemical properties of TiO_2-RuO_2

composites coupled with high surface area, which improved the photocatalytic performance. XRD confirmed the presence of the anatase phase of TiO_2 and the crystalline RuO_2 phase. DRS showed improved band and visible light absorption properties compared to the commercially available TiO_2. Results obtained from physicochemical and electrochemical characterization revealed the high potential of the TiO_2-RuO_2-20 to split water for hydrogen generation compared to all the other samples. This can be attributed to an enhanced heterojunction between the TiO_2 and RuO_2 phases, resulting in a practical synergistic effect in electron transfer, and can further be said to be due to a combination of the suitable composition of TiO_2 and RuO_2 in the composite. This was observed in the improved light absorption properties, reduced band gap, double reduction potential, low photoluminescence emission, low solution resistance, and high current density as compared to the other materials and the pristine and commercial TiO_2. Water splitting experiment for hydrogen production in the presence of solar light confirmed the excellent performance of TiO_2-RuO_2-20, which yielded a significant amount of hydrogen gas, 1794.8 $\mu molg^{-1}h^{-1}$, over 3 h of activity. This amount far exceeded the yield observed for the RuO_2 only (21.9 $\mu molg^{-1}h^{-1}$) and the commercially available TiO_2 (641.0 $\mu molg^{-1}h^{-1}$). This confirms the effectiveness and low amount of ruthenium required in fabricating highly effective catalysts for photocatalysis, and the single-step, low-cost method offers an advantage in obtaining cost-effective materials for efficient hydrogen generation.

Supporting information

SEM images, XRD spectra, Raman spectra, XPS spectra, Band gap, Photoluminescence spectra, Mott–Schottky plot, Water splitting mechanism

Data availability

Data will be made available on reasonable request.

Author contributions

M.D.A. did experiment, characterization, and wrote the manuscript. G. P. took and analyzed TEM images. S. M. performed BET experiment. B.P.B. supervised the research, revised the manuscript, and funded this project.

Conflict of interest

The authors declare no competing financial Interest.

Acknowledgements

This work is funded by the National Science Foundation-Collaborative Research and Education in Advanced Materials (NSF-2425119). The HR-TEM was performed at the Joint School of Nanoscience and Nanoengineering, a member of the Southeastern Nanotechnology Infrastructure Corridor (SENIC) and National Nanotechnology Coordinated Infrastructure (NNCI), supported by the NSF (grant ECCS-1542174). The authors acknowledge the DOD HBCU/MSI instrumentation award (contract #: W911NF1910522) to acquire HR-TEM (JEOL 2100PLUS) with STEM/EDS capability. Thanks Mr. Rabin Dahal for SEM imaging.

Notes and References

1 O. Awogbemi and D. V. Von Kallon, *Fuel Commun.*, 2023, **17**, 100099.

2 S. Singh, S. Jain, V. Ps, A. K. Tiwari, M. R. Nouni, J. K. Pandey and S. Goel, *Renew. Sustain. Energy Rev.*, 2015, **51**, 623–633.

3 National Hydrogen Association, *New York State Energy Res. Dev. Auth.*, 2010, 1–2.

4 H. Idriss, *Curr. Opin. Chem. Eng.*, 2020, **29**, 74–82.

5 M. T. Uddin, O. Babot, L. Thomas, C. Olivier, M. Redaelli, M. D'Arienzo, F. Morazzoni, W. Jaegermann, N. Rockstroh, H. Junge and T. Toupance, *J. Phys. Chem. C*, 2015, **119**, 7006–7015.

6 C. Yuan, Y. Shen, C. Zhu, P. Zhu, F. Yang, J. Liu and C. An, *ACS Sustain. Chem. Eng.*, 2022, **10**, 10311–10317.

7 M. D. Ashie and B. P. Bastakoti, *Small*, 2024, **29**, 2310927.

8 M. S. Mirghani, *J. Exp. Nanosci.*, 2021, **16**, 52–62.

9 L. Díaz, V. D. Rodríguez, M. González-Rodríguez, E. Rodríguez-Castellón, M. Algarra, P. Núñez and E. Moretti, *Inorg. Chem. Front.*, 2021, **8**, 3491–3500.

10 M. D. Ashie, K. West, R. Dahal, B. P. Bastakoti, Microscopy and Microanalysis, 2024, **30**, 543–544.

11 S. De, S. Roy and G. C. Nayak, *Mater. Today Nano*, 2023, **22**, 100337.

12 H. Zhang, P. Sun, X. Fei, X. Wu, Z. Huang, W. Zhong, Q. Gong, Y. Zheng, Q. Zhang, S. Xie, G. Fu and Y. Wang, *Nat. Commun.*, DOI:10.1038/s41467-024-48866-1.

13 M. Dahl, Y. Liu and Y. Yin, *Chem. Rev.*, 2014, **114**, 9853–9889.

14 H. Khan and M. U. H. Shah, *J. Environ. Chem. Eng.*, 2023, **11**, 111532.

15 Y. Wang, H. Suzuki, J. Xie, O. Tomita, D. J. Martin, M. Higashi, D. Kong, R. Abe and J. Tang, *Chem. Rev.*, 2018, **118**, 5201–5241.

16 M. T. Uddin, Y. Nicolas, C. Olivier, T. Toupance, M. M. Müller, H. J. Kleebe, K. Rachut, J. Ziegler, A. Klein and W. Jaegermann, *J. Phys. Chem. C*, 2013, **117**, 22098–22110.

17 B. P. Bastakoti, R. R. Salunkhe, J. Ye and Y. Yamauchi, *Phys. Chem. Chem. Phys.*, DOI:10.1039/c4cp01118j.

18 G. Han, G. Li, J. Huang, C. Han, C. Turro and Y. Sun, *Nat. Commun.*, 2022, **13**, 1–10.

19 J. H. Tang, G. Han, G. Li, K. Yan and Y. Sun, *iScience*, 2022, **25**, 104064.

20 M. M. Heravi, M. Ghavidel and L. Mohammadkhani, *RSC Adv.*, 2018, **8**, 27832–27862.

21 N. Basma, P. L. Cullen, A. J. Clancy, M. S. P. Shaffer, N. T. Skipper, T. F. Headen and C. A. Howard, *Mol. Phys.*, 2019, **117**, 3353–3363.

22 H.-H. C. and S.-W. K. Ahmed F. M. EL-Mahdy, Ahmed M. Elewa, Sheng-Wen Huang, 2020, DOI: 10.1002/adom.202000641.

23 W. Song, K. Leung, Q. Shao, K. J. Gaskell and J. E. Reutt-Robey, *J. Phys. Chem. C*, 2016, **120**, 22979–22988.

24 M. Sałdyka, Z. Mielke and K. Haupa, *Spectrochim. Acta - Part A Mol. Biomol. Spectrosc.*, 2018, **190**, 423–432.

25 J. A. Clark, A. Murray, J. M. Lee, T. S. Autrey, A. D. Collord and H. W. Hillhouse, *J. Am. Chem. Soc.*, 2019, **141**, 298–308.

26 C. Zhao, Q. Li, Y. Xie, L. Zhang, X. Xiao, D. Wang, Y. Jiao, C. A. Hurd Price, B. Jiang and J. Liu, *J. Mater. Chem. A*, 2020, **8**, 305–312.

27 M. Šćepanović, S. Aškrabić, V. Berec, A. Golubović, Z. Dohčević-Mitrović, A. Kremenović and Z. V. Popović, *Acta Phys. Pol. A*, 2009, **115**, 771–774.

28 M. Amin, J. Tomko, J. J. Naddeo, R. Jimenez, D. M. Bubb, M. Steiner, J. Fitz-Gerald and S. M. O'Malley, *Appl. Surf. Sci.*, 2015, **348**, 30–37.

29 J. Park, J. W. Lee, B. U. Ye, S. H. Chun, S. H. Joo, H. Park, H. Lee, H. Y. Jeong, M. H. Kim and J. M. Baik, *Sci. Rep.*, 2015, **5**, 1–10.

30 S. Sarkar, D. Mukherjee, R. Harini and G. Nagaraju, *J. Mater. Sci.*, 2022, **57**, 7680–7693.

31 B. Bharti, S. Kumar, H. N. Lee and R. Kumar, *Sci. Rep.*, 2016, **6**, 1–12.

32 C. Mun, J. J. Ehrhardt, J. Lambert and C. Madic, *Appl. Surf. Sci.*, 2007, **253**, 7613–7621.

33 T. R. Gengenbach, G. H. Major, M. R. Linford and C. D. Easton, *J. Vac. Sci. Technol. A Vacuum, Surfaces, Film.*, DOI:10.1116/6.0000682.

34 M. C. Biesinger, L. W. M. Lau, A. R. Gerson and R. S. C. Smart, *Appl. Surf. Sci.*, 2010, **257**, 887–898.

35 D. Tuschel, *Spectrosc. (Santa Monica)*, 2016, **31**, 14–21.

36 Y. Qin, T. Yu, S. Deng, X. Y. Zhou, D. Lin, Q. Zhang, Z. Jin, D. Zhang, Y. B. He, H. J. Qiu, L. He, F. Kang, K. Li and T. Y. Zhang, *Nat. Commun.*, DOI:10.1038/s41467-022-31468-0.

37 N. Deka, T. E. Jones, L. J. Falling, L. E. Sandoval-Diaz, T. Lunkenbein, J. J. Velasco-Velez, T. S. Chan, C. H. Chuang, A. Knop-Gericke and R. V. Mom, *ACS Catal.*, 2023, **13**, 7488–7498.

38 F. Mousli, A. Chaouchi, M. Jouini, F. Maurel, A. Kadri and M. M. Chehimi, *Catalysts*, DOI:10.3390/catal9070578.

39 S. Shen, X. Li, Y. Zhou, L. Han, Y. Xie, F. Deng, J. Huang, Z. Chen, Z. Feng, J. Xu and F. Dong, *J. Mater. Sci. Technol.*, 2023, **155**, 148–159.

40 H. K. Kim, I. H. Yu, J. H. Lee, T. J. Park and C. S. Hwang, *ACS Appl. Mater. Interfaces*, 2013, **5**, 1327–1332.

41 G. Lakshminarayana, I. V. Kityk and T. Nagao, *J. Mater. Sci. Mater. Electron.*, 2016, **27**, 10791–10797.

42 Z. J. Yang, J. Li, R. F. Linghu, X. L. Cheng and X. D. Yang, *Can. J. Phys.*, 2012, **90**, 441–448.

43 Z. Zan, X. Li, X. Gao, J. Huang, Y. Luo and L. Han, *Wuli Huaxue Xuebao/ Acta Phys. - Chim. Sin.*, 2023, **39**, 1–13.

44 X. Li, T. Han, Y. Zhou, M. Wang, Z. Tian, F. Deng, Y. Luo, Y. Xie, J. Huang, L. Han, Z. Chen, Z. Feng and W. Chen, *Appl. Catal. B Environ.*, 2024, **350**, 123913.

45 S. Zhao, S. S. Shen, L. Han, B. C. Tian, N. Li, W. Chen and X. B. Li, *Rare Met.*, 2024, **43**, 4038–4055.

46 X. Li, B. Kang, F. Dong, Z. Zhang, X. Luo, L. Han, J. Huang, Z. Feng, Z. Chen, J. Xu, B. Peng and Z. L. Wang, *Nano Energy*, 2021, **81**, 105671.

Data availability

Data will be made available on reasonable request.